nature immunology

Receptor interacting protein kinase 2–mediated mitophagy regulates inflammasome activation during virus infection

Christopher Lupfer[1], Paul G Thomas[1], Paras K Anand[1], Peter Vogel[2], Sandra Milasta[1], Jennifer Martinez[1], Gonghua Huang[1], Maggie Green[1], Mondira Kundu[3], Hongbo Chi[1], Ramnik J Xavier[4–6], Douglas R Green[1], Mohamed Lamkanfi[7,8], Charles A Dinarello[9], Peter C Doherty[1,10] & Thirumala-Devi Kanneganti[1]

NOD2 receptor and the cytosolic protein kinase RIPK2 regulate NF-κB and MAP kinase signaling during bacterial infections, but the role of this immune axis during viral infections has not been addressed. We demonstrate that *Nod2*$^{-/-}$ and *Ripk2*$^{-/-}$ mice are hypersusceptible to infection with influenza A virus. *Ripk2*$^{-/-}$ cells exhibited defective autophagy of mitochondria (mitophagy), leading to enhanced mitochondrial production of superoxide and accumulation of damaged mitochondria, which resulted in greater activation of the NLRP3 inflammasome and production of IL-18. RIPK2 regulated mitophagy in a kinase-dependent manner by phosphorylating the mitophagy inducer ULK1. Accordingly, *Ulk1*$^{-/-}$ cells exhibited enhanced mitochondrial production of superoxide and activation of caspase-1. These results demonstrate a role for NOD2-RIPK2 signaling in protection against virally triggered immunopathology by negatively regulating activation of the NLRP3 inflammasome and production of IL-18 via ULK1-dependent mitophagy.

Seasonal influenza A virus (IAV) epidemics are a major cause of morbidity and economic loss, with annual mortality rates estimated in the 9,000–45,000 range for the United States alone[1]. In addition, global pandemics of IAV strains with new antigens that emerge from avian and domestic swine reservoirs can result in deaths of millions. The catastrophic 1918 H1N1 pandemic was characterized by an unusually high incidence of rapid lethality in otherwise healthy young adults[2]. More recently, similar pathological profiles have been documented for infections caused by the highly virulent avian H5N1 IAV strains[3,4]. In both humans and animal models, infections with these highly pathogenic strains were characterized by rapid onset of a proinflammatory 'cytokine storm' that damaged lung epithelium, resulting in edema and hemorrhage. Relative to the host responses induced by low-pathogenicity influenza viruses, host responses to infection with the 1918 H1N1 or highly pathogenic H5N1 viruses are associated with markedly greater neutrophil and macrophage infiltration and elevated amounts of cytokines and chemokines, including IL-1β, IFN-γ and tumor necrosis factor (TNF)[4–6]. Thus, it is increasingly clear that overt inflammation during IAV infection contributes substantially to morbidity and mortality.

Signaling pathways that regulate the innate immune response to IAV infection are now being defined, with obvious roles for the endocytic Toll-like receptors TLR3 (ref. 7) and TLR7 (ref. 8), and the cytosolic receptor RIG-I (ref. 9). Recently, members of the Nod-like receptor (NLR) family have also been shown to recognize IAV in the cytosolic compartment[10–12]. NLRP3 detects IAV infection through multiple mechanisms, including ion flux generated by the virus-encoded M2 ion channel[11] and via the recognition of viral RNA[10,13]. These signals serve to activate the inflammasome, a macromolecular complex consisting of caspase-1, the adaptor protein ASC and NLRP3 (ref. 14). Inflammasome activation leads to the cleavage of many substrates, including pro-IL-1β and pro-IL-18, and the initiation of the proinflammatory form of cell death known as pyroptosis[15].

Autophagy is a cellular process where cytoplasmic double-membrane vesicles are formed and engulf cytoplasmic contents. Several forms of autophagy exist, including macroautophagy, where long-lived proteins or organelles are engulfed and degraded for recycling[16]. Recently macroautophagy has been shown to be a critical modulator of inflammasome activation[17], but it is unknown whether this is applicable during viral infection. Another subset of the autophagic process is known as mitophagy, where mitochondria are specifically degraded in response to damage or developmental cues[18,19]. Finally, xenophagy is an innate immune mechanism, where invading cytosolic pathogens are captured and degraded to prevent their spread and for antigen presentation to initiate adaptive immunity[20,21].

[1]Department of Immunology, St. Jude Children's Research Hospital, Memphis, Tennessee, USA. [2]Veterinary Pathology Core, St. Jude Children's Research Hospital, Memphis, Tennessee, USA. [3]Department of Pathology, St. Jude Children's Research Hospital, Memphis, Tennessee, USA. [4]Gastrointestinal Unit and Center for the Study of Inflammatory Bowel Disease, Harvard Medical School, Boston, Massachusetts, USA. [5]Center for Computational and Integrative Biology, Massachusetts General Hospital, Harvard Medical School, Boston, Massachusetts, USA. [6]The Broad Institute of Massachusetts Institute of Technology and Harvard, Cambridge, Massachusetts, USA. [7]Department of Biochemistry, Ghent University, Ghent, Belgium. [8]Department of Medical Protein Research, Vlaams Instituut voor Biotechnologie, Ghent, Belgium. [9]Department of Medicine, University of Colorado Denver, Aurora, Colorado, USA. [10]Department of Microbiology and Immunology, University of Melbourne, Parkville, Victoria, Australia. Correspondence should be addressed to T.-D.K. (thirumala-devi.kanneganti@stjude.org).

Received 27 November 2012; accepted 25 January 2013; published online 24 March 2013; doi:10.1038/ni.2563

RIPK2 (also known as RIP2 or RICK) is a critical mediator of inflammatory responses to bacterial infections, where it is activated by the NLRs NOD1 and NOD2. RIPK2 is involved in the induction of xenophagy in response to bacterial infections[20,22,23]. Furthermore, the sensing of bacterial peptidoglycan components activates the NOD1-NOD2-RIPK2 axis and signals through the transcription factor NF-κB and through MAP kinase (MAPK) to activate inflammatory cells and to promote secretion of proinflammatory cytokines and chemokines[24]. Although NOD2 regulates production of type I interferon during viral infections independently of RIPK2 (refs. 25,26), putative roles of RIPK2 during IAV infection have not been determined. Here we demonstrate that *Ripk2*$^{-/-}$ mice are hypersusceptible to IAV infection. RIPK2 dampens activation of the inflammasome and secretion of IL-18, which contribute critically to disease progression. Mechanistically, increases in the production of IL-18 and activation of the inflammasome are a consequence of defective induction of mitophagy in IAV-infected *Ripk2*$^{-/-}$ mice and immune cells. Finally we demonstrate that activation of the critical autophagy inducer ULK1 is lower in *Ripk2*$^{-/-}$ cells and that *Ulk1*$^{-/-}$ cells also exhibited greater inflammasome activation and lower mitophagy relative to wild-type controls. Our results highlight a previously unknown RIPK2-dependent signaling network that negatively regulates inflammasome activation through mitophagy during viral infection.

RESULTS

RIPK2 protects against severe IAV infection

To examine the potential role of NOD2 and RIPK2 in the immune response to IAV infection, we challenged wild-type, *Nod2*$^{-/-}$ and *Ripk2*$^{-/-}$ mice intranasally with the virulent influenza A/Puerto Rico/8/34 (PR8) H1N1 virus and monitored survival over time. Relative to wild-type controls, *Nod2*$^{-/-}$ and *Ripk2*$^{-/-}$ mice had significantly higher mortality rates (**Fig. 1a**). Although signs of pathological damage to the lungs of wild-type mice were minimal by day 2 after PR8 inoculation, lung sections of both knockout mouse lines showed marked pathological changes, characterized by greater pulmonary airway obstruction and increased cell death on days 2 and 7 after infection (**Fig. 1b–d** and data not shown). Moreover, airway obstruction of IAV-infected *Ripk2*$^{-/-}$ mice consisted mainly of neutrophils (**Fig. 1e**). Whereas neutrophil counts were elevated in the *Ripk2*$^{-/-}$ whole lung on days 2 and 7, we observed no increases in the numbers of other myeloid cells (**Fig. 1f,g**). Despite the greater susceptibility of *Ripk2*$^{-/-}$ mice to IAV infection, lung virus titers were comparable to those in wild-type controls (**Fig. 1h**). Thus, NOD2 and RIPK2 protect against severe IAV infection, although this is not correlated with the extent of virus replication.

RIPK2 regulates IFN-γ and IL-18

Given that the inflammatory response to IAV is thought to contribute to mortality[3,4], we investigated the role of RIPK2 in cytokine production. To this end, we collected whole lung homogenates on days 2 and 7 after intranasal challenge of wild-type and *Ripk2*$^{-/-}$ mice with the PR8 virus and determined the extent of inflammatory mediator production by enzyme-linked immunosorbent assay (ELISA). Although RIPK2 regulates production of IL-6 and TNF during bacterial infections[27], we observed no significant differences in the amounts of these cytokines in lungs of virus-infected wild-type and *Ripk2*$^{-/-}$ mice (**Fig. 2a**). In contrast, IFN-γ, a known mediator of inflammation in viral immunity[28], and IL-18 were significantly upregulated in *Ripk2*$^{-/-}$ mice (**Fig. 2b**). Originally, IL-18 had been identified as an IFN-γ–inducing cytokine[29], suggesting that production of IFN-γ might be consequential to more IL-18 release in IAV-infected *Ripk2*$^{-/-}$ mice. Previous studies have shown the chemokines CCL2 (MCP-1) and CXCL10 (IP-10) are induced by IL-18 and IFN-γ[30]; accordingly,

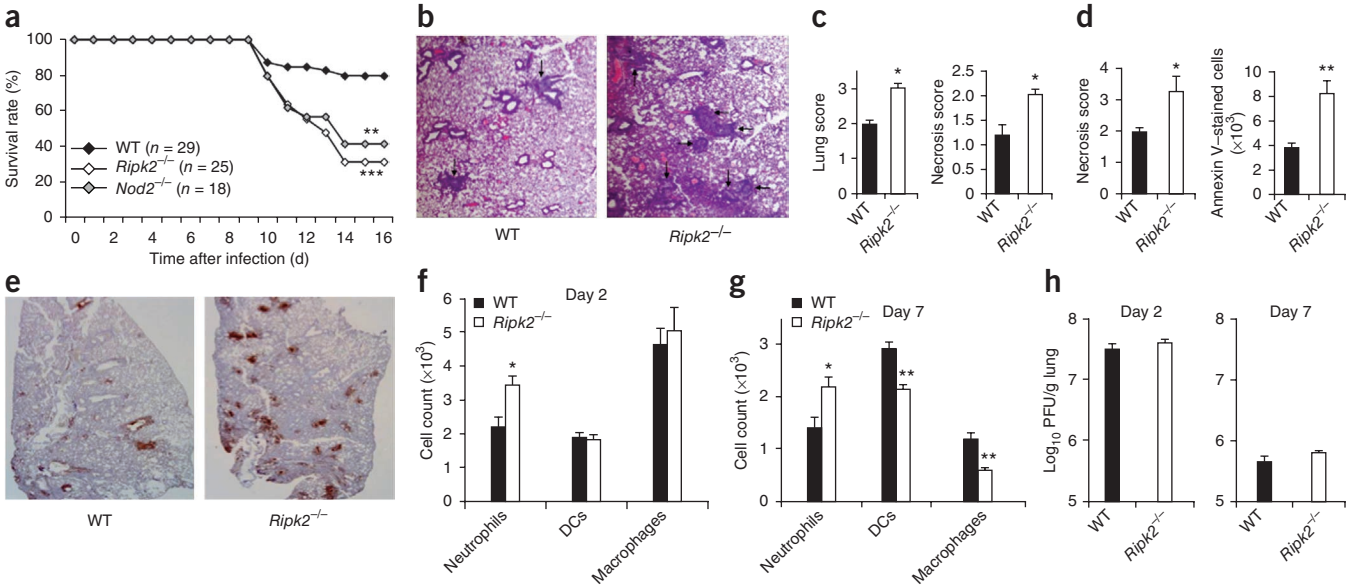

Figure 1 RIPK2 deficiency leads to hyperinflammation. (**a**) Survival rate of wild-type mice (WT) and indicated knockout mice after intranasal infection with 750 plaque forming units (PFU) of the PR8 virus. (**b**) Hematoxylin and eosin (H&E)-stained lung sections from mice infected with PR8 virus on day 2. Arrows indicate cellular infiltrates and necrotic debris occluding the airways. Original magnification, ×40. (**c**) Disease severity ('lung score') and extent of cell death (necrosis score) on day 2 after infection based on analysis of H&E-stained lung sections. (**d**) Necrosis score on day 7, estimated visually from H&E-stained lung sections, and flow cytometry analysis for annexin V–stained lung cell populations. (**e**) Immunohistochemistry staining of neutrophils occluding the airways of PR8-infected mice. Original magnification, ×20. (**f**,**g**) Flow cytometry analysis of neutrophil, dendritic cell (DC) and macrophage cell numbers on days 2 and 7. (**h**) Pulmonary viral titers on days 2 and 7 after infection in *Ripk2*$^{-/-}$ and WT mice. $^{*}P < 0.05$, $^{**}P < 0.01$, $^{***}P < 0.001$ (log-rank test (**a**) and unpaired two-sided Student's *t*-test (**c**,**d**,**f**,**g**). Data are pooled from three experiments (**a**,**f**–**h**; mean ± s.e.m. in **f**–**h**; $n = 10$–12 mice total) or are representative of three experiments (**b**–**e**; mean ± s.e.m.; $n = 3$–5 mice per experiment).

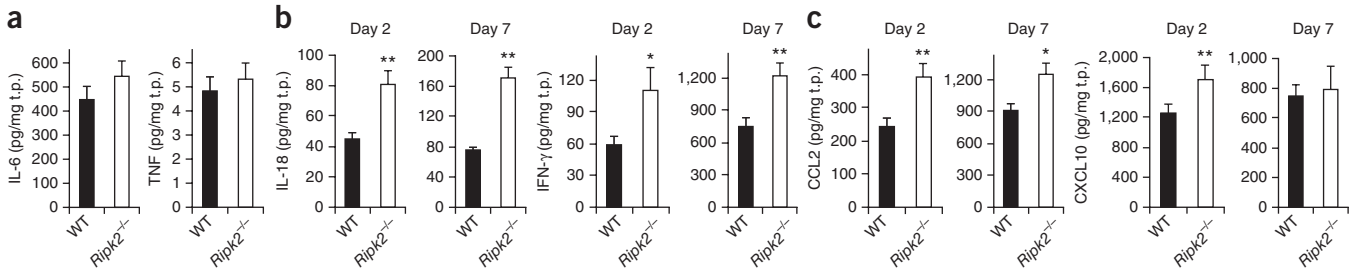

Figure 2 RIPK2 modulates cytokine and chemokine production. (**a**–**c**) Supernatants of whole lung homogenates taken on days 2 and 7 after infection of wild-type mice (WT) and *Ripk2*$^{-/-}$ mice with the PR8 virus were analyzed for IL-6 and TNF (day 2; **a**), IL-18 and IFN-γ (**b**), and indicated chemokines (**c**). $*P < 0.05$, $**P < 0.01$ (unpaired two-sided Student's *t*-test). Data were normalized for total protein (t.p.) from lung homogenates. Data are pooled from three experiments (mean ± s.e.m.; $n = 10$–12 mice total).

we observed elevated production of both CCL2 and CXCL10 in IAV-infected *Ripk2*$^{-/-}$ mice (**Fig. 2c**). These results indicate that greater susceptibility to IAV infection in *Ripk2*$^{-/-}$ mice is associated with exacerbated production of IL-18 and IFN-γ.

IL-18 antagonism in *Ripk2*$^{-/-}$ mice improves survival

We hypothesized that the higher production of IL-18 was responsible for increased inflammation and mortality during IAV infection of *Ripk2*$^{-/-}$ mice. To test this, we injected *Ripk2*$^{-/-}$ mice intraperitoneally with anti–IL-18 neutralizing antibody 3 h before infection with PR8. This treatment resulted in significantly lower amounts of IL-18, IFN-γ and CCL2 in the lungs of IAV-infected *Ripk2*$^{-/-}$ mice (**Fig. 3a**). This was followed by moderately fewer of the chemokines CXCL10, CXCL1 (KC) and CCL3 (MIP-1α) ($P = 0.15$, 0.30 and 0.22, respectively; **Supplementary Fig. 1a**). Furthermore, IL-18 neutralization dampened virus-induced lung pathology and airway neutrophilia (**Fig. 3b**,**c** and **Supplementary Fig. 1b**), and significantly improved survival (**Fig. 3d**). These results suggest that the higher production of IL-18 drives elevated morbidity and mortality in IAV-infected *Ripk2*$^{-/-}$ mice. To confirm the critical role of IL-18 in this process, we generated mice lacking both RIPK2 and IL-18 (*Ripk2*$^{-/-}$*Il18*$^{-/-}$ mice) and challenged these mice with a lethal dose of IAV. As with *Ripk2*$^{-/-}$ mice receiving IL-18–neutralizing antibodies, genetic ablation of IL-18 rescued the hypersensitive response of *Ripk2*$^{-/-}$ mice; tissue neutrophil infiltration and mortality rates returned to levels comparable to those of infected wild-type mice (**Fig. 3e**,**f**). These results demonstrate a critical role for elevated IL-18 production increasing morbidity and mortality in IAV-infected *Ripk2*$^{-/-}$ mice.

Immune and lung cells contribute to elevated IL-18

To identify the cellular compartments that contribute to RIPK2-mediated modulation of IL-18, we generated bone marrow chimeras that

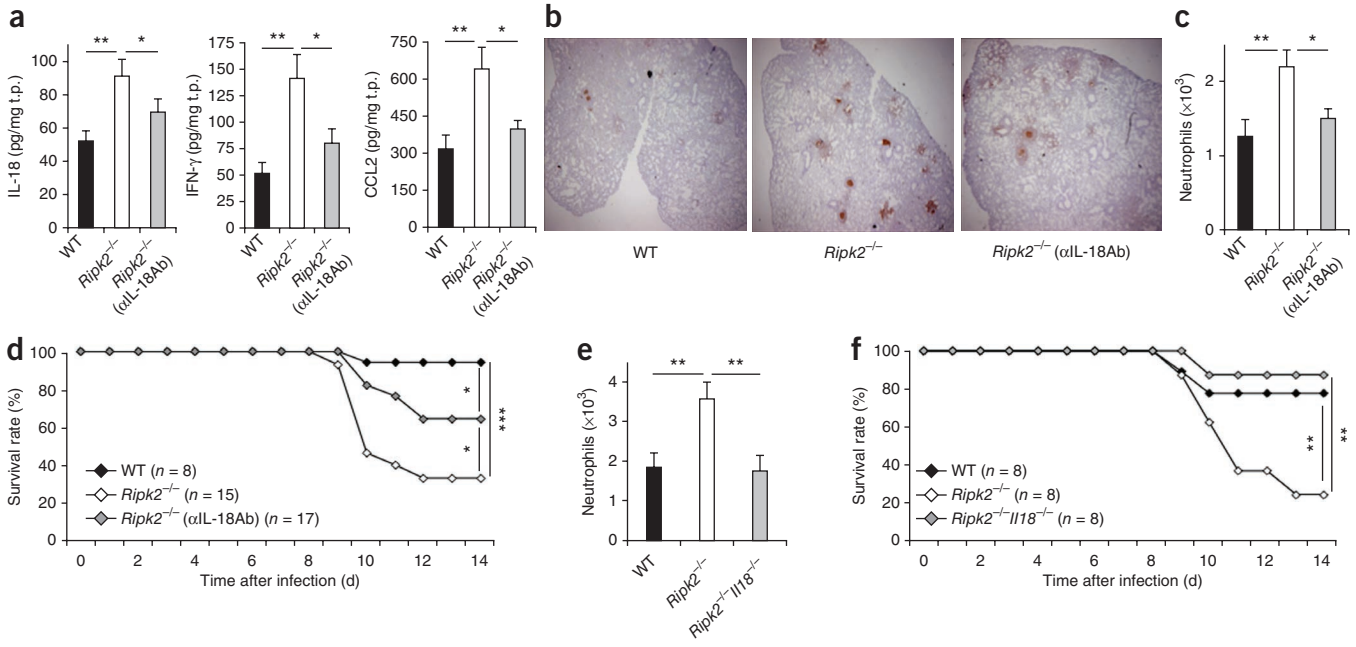

Figure 3 IL-18 mediates hyperinflammation in *Ripk2*$^{-/-}$ mice. (**a**–**c**) Analysis on day 2 after infection with PR8 virus of wild-type mice (WT) or *Ripk2*$^{-/-}$ mice injected intraperitoneally with control rabbit serum and *Ripk2*$^{-/-}$ mice injected intraperitoneally with anti–IL-18 neutralizing antiserum (αIL-18Ab) 3 h before infection, for IL-18, IFN-γ and CCL2 amounts in whole lung homogenates (**a**; t.p., total protein), and for neutrophil numbers by immunohistochemistry (**b**) and by flow cytometry (**c**). Original magnification, ×20. (**d**) Analysis of survival of indicated mice. (**e**) Neutrophil numbers in WT, *Ripk2*$^{-/-}$ and *Ripk2*$^{-/-}$*Il18*$^{-/-}$ mice on day 2 after PR8 infection. (**f**) Survival of *Ripk2*$^{-/-}$*Il18*$^{-/-}$, *Ripk2*$^{-/-}$ and WT mice. $*P < 0.05$, $**P < 0.01$, $***P < 0.001$ (one-way ANOVA with Tukey's *post-hoc* test (**a**,**c**,**e**) and log-rank test (**d**,**f**)). Data are representative of two independent experiments (mean ± s.e.m.; $n = 6$–8 mice per experiment).

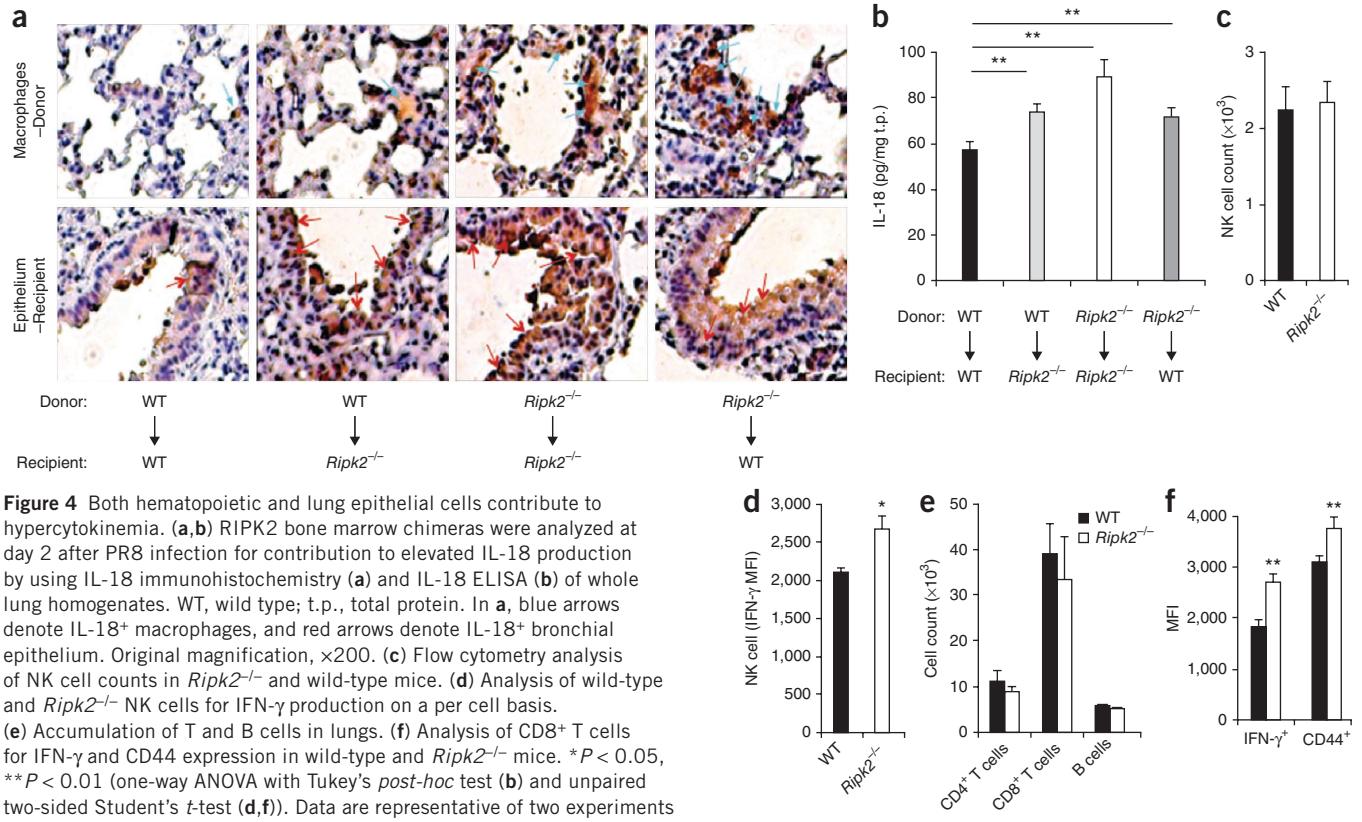

Figure 4 Both hematopoietic and lung epithelial cells contribute to hypercytokinemia. (**a**,**b**) RIPK2 bone marrow chimeras were analyzed at day 2 after PR8 infection for contribution to elevated IL-18 production by using IL-18 immunohistochemistry (**a**) and IL-18 ELISA (**b**) of whole lung homogenates. WT, wild type; t.p., total protein. In **a**, blue arrows denote IL-18$^+$ macrophages, and red arrows denote IL-18$^+$ bronchial epithelium. Original magnification, ×200. (**c**) Flow cytometry analysis of NK cell counts in *Ripk2*$^{-/-}$ and wild-type mice. (**d**) Analysis of wild-type and *Ripk2*$^{-/-}$ NK cells for IFN-γ production on a per cell basis. (**e**) Accumulation of T and B cells in lungs. (**f**) Analysis of CD8$^+$ T cells for IFN-γ and CD44 expression in wild-type and *Ripk2*$^{-/-}$ mice. $^*P < 0.05$, $^{**}P < 0.01$ (one-way ANOVA with Tukey's *post-hoc* test (**b**) and unpaired two-sided Student's *t*-test (**d**,**f**)). Data are representative of two experiments (**a**,**b**,**f**) or three experiments (**c**–**e**) (mean ± s.e.m.; $n = 6$–8 mice per experiment).

selectively expressed RIPK2 in the radiation-sensitive (donor bone marrow) or radiation-resistant (recipient lung) compartments. We infected these chimeric mice intranasally with PR8 and assessed IL-18 production by immunohistochemistry and ELISA. Both *Ripk2*$^{-/-}$ hematopoietic and non-immune (likely lung epithelial) cells contributed to higher production of IL-18 in the pulmonary tract of IAV-infected *Ripk2*$^{-/-}$ mice (**Fig. 4a**,**b** and **Supplementary Fig. 2a**).

Innate and adaptive lymphocytes are hyperactivated

We next examined the cellular populations that were responsible for the larger amounts of IFN-γ observed in *Ripk2*$^{-/-}$ mice compared to wild-type mice. Both NK cells and CD8$^+$ T cells isolated from PR8-infected *Ripk2*$^{-/-}$ mice produced more IFN-γ per cell and were more highly activated, although the absolute numbers of these cells remained similar to those in wild-type mice (**Fig. 4c**–**f**, and **Supplementary Fig. 2b**–**d**). These results indicate that larger amounts of IL-18 in *Ripk2*$^{-/-}$ mice subsequently lead to more production of IFN-γ from innate and adaptive cell populations.

NOD2-RIPK2 axis regulates caspase-1 activation and IL-18

NOD2 has been reported to regulate type I interferon during IAV infection[25,26]. Although we confirmed the reported defect in the production of type I interferon after IAV infection of *Nod2*$^{-/-}$ alveolar macrophages ($P = 0.018$; data not shown), *Ripk2*$^{-/-}$ macrophages produced type I interferon (IFN-β) protein in amounts similar to those of wild-type cells ($P = 0.469$, data not shown), suggesting that differences in type I interferon signaling are unlikely to account for the observed hypersensitive phenotype of *Ripk2*$^{-/-}$ mice. Similarly, we found no differences in activation of NF-κB (pIκBα) and MAPK (p-Erk) pathways in IAV-infected *Ripk2*$^{-/-}$ bone marrow–derived dendritic cells (BMDCs; data not shown). We therefore analyzed processes directly regulating maturation of IL-18 rather than abundance of transcripts encoding IL-18. Unlike most cytokines, IL-1β and IL-18 are produced as pro-peptides that require proteolytic maturation by the cysteine protease caspase-1 to be released in their biologically active forms[31]. Notably, both activation of caspase-1 and release of mature IL-18 were markedly greater in PR8 infected *Ripk2*$^{-/-}$ and *Nod2*$^{-/-}$ BMDCs compared to wild-type controls (**Fig. 5a**,**b**). In agreement with the observed greater caspase-1 activation, we also detected more IL-1β in *Ripk2*$^{-/-}$ BMDCs compared to wild-type controls. We therefore reexamined lung homogenates from *in vivo* samples for IL-1β. However, low amounts of IL-1β likely confounded detection of differences in this cytokine *in vivo* (**Supplementary Fig. 3a**). Next, we examined activation of caspase-1 in response to other pathogens. We observed that the X31 low-pathogenicity influenza A virus also elicited higher caspase-1 activation in *Ripk2*$^{-/-}$ BMDCs (**Supplementary Fig. 3b**). We also examined inflammasome activation during infection with bacteria known to activate the RIPK2 signaling pathway. Infection with *Listeria monocytogenes* did not augment processing of caspase-1 and production of IL-18 in *Ripk2*$^{-/-}$ and *Nod2*$^{-/-}$ BMDCs (**Fig. 5c**,**d**). Enhancement of inflammasome activation by IAV in *Ripk2*$^{-/-}$ BMDCs was dependent on NLRP3, as the NLRP3-specific inhibitor glyburide[32] significantly inhibited activation of caspase-1 and production of IL-18 (**Fig. 5e**,**f**). In the case of *Listeria* infection, the AIM2 inflammasome has a predominant role in inflammasome activation[33]. In agreement, *Aim2*$^{-/-}$ BMDCs exhibited nearly complete impairment in caspase-1 activation after infection with *Listeria* (**Fig. 5g**). These data indicate that enhanced activation of the NLRP3 inflammasome occurs in *Ripk2*$^{-/-}$ BMDCs during IAV infection but not during *Listeria* infection, indicating that this pathway is not involved in global disregulation of inflammasome activation, but specific to the NLRP3 inflammasome.

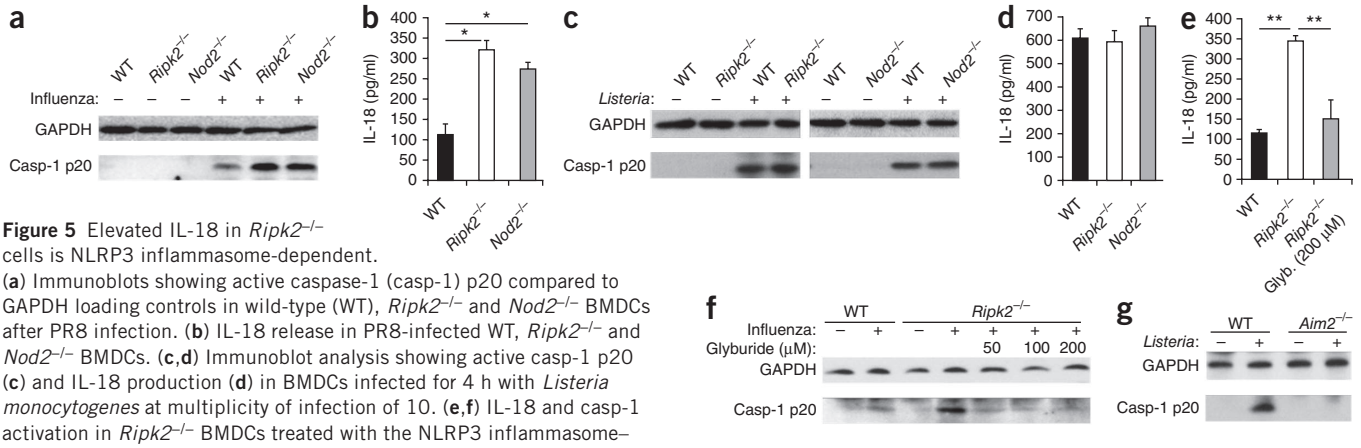

Figure 5 Elevated IL-18 in *Ripk2*$^{-/-}$ cells is NLRP3 inflammasome-dependent. (**a**) Immunoblots showing active caspase-1 (casp-1) p20 compared to GAPDH loading controls in wild-type (WT), *Ripk2*$^{-/-}$ and *Nod2*$^{-/-}$ BMDCs after PR8 infection. (**b**) IL-18 release in PR8-infected WT, *Ripk2*$^{-/-}$ and *Nod2*$^{-/-}$ BMDCs. (**c**,**d**) Immunoblot analysis showing active casp-1 p20 (**c**) and IL-18 production (**d**) in BMDCs infected for 4 h with *Listeria monocytogenes* at multiplicity of infection of 10. (**e**,**f**) IL-18 and casp-1 activation in *Ripk2*$^{-/-}$ BMDCs treated with the NLRP3 inflammasome–specific inhibitor glyburide (glyb.) during PR8 infection. (**g**) Immunoblot analysis of casp-1 p20 during *Listeria* infection of WT and *Aim2*$^{-/-}$ BMDCs. $^{*}P < 0.01$, $^{**}P < 0.001$ (one-way ANOVA with Tukey's *post-hoc* test). Data are representative of six experiments (**a**,**b**) or three experiments (**c**–**g**) (mean ± s.d.; $n = 2$–3 replicates per experiment).

RIPK2 regulates the NLRP3 inflammasome through autophagy

To determine the mechanism by which RIPK2 dampens inflammasome activation, we first assessed the effect of RIPK2 overexpression on maturation of caspase-1 and release of IL-18 in transfected 293T cells. In agreement with published reports[34], overexpressed RIPK2 interacted with caspase-1, but overexpression enhanced, rather than inhibited, processing of caspase-1 and release of IL-18 (data not shown), indicating that overexpression of RIPK2 cannot directly inhibit inflammasome activation. Because *Ripk2*$^{-/-}$ BMDCs do not display a global defect in inflammasome activation (**Fig. 5**), this suggests that RIPK2 may modulate caspase-1 indirectly in our model. In this regard, autophagy has been described to negatively regulate inflammasome activation during bacterial infections[17,35,36]. We therefore hypothesized that *Ripk2*$^{-/-}$ and *Nod2*$^{-/-}$ BMDCs might be defective in the induction of autophagy in response to IAV infection. LC3 lipidation is an important step in the formation of autophagosomes. Therefore, one method to examine autophagic activity is to examine the amount of LC3-II (lipidated form). In agreement with our hypothesis, *Ripk2*$^{-/-}$ and *Nod2*$^{-/-}$ BMDCs had substantially less LC3-II protein than wild-type BMDCs infected with either PR8 or X31 (**Fig. 6a** and **Supplementary Fig. 4a**). Turnover of autophagosomes, which results from their fusion with lysosomes, was not affected by IAV infection in wild-type or *Ripk2*$^{-/-}$ BMDCs as treatment with the lysosomal fusion inhibitor chloroquine resulted in the expected accumulation of LC3^{+} puncta by immunofluorescence and LC3-II by immunoblot (**Fig. 6b**,**c** and **Supplementary Fig. 4b**). Finally, we counted autophagosomes by electron microscopy and determined that after IAV infection *Ripk2*$^{-/-}$ BMDCs had significantly fewer autophagosomes than wild-type BMDCs ($P = 0.035$; **Supplementary Fig. 4c**–**e**). To establish the potential role of autophagy induction in response to IAV infection in regulating activation of caspase-1, we compared wild-type, RIPK2- and ATG7-deficient bone marrow–derived macrophages, which lack a critical component of the autophagy machinery in myeloid cells. Both RIPK2- and ATG7-deficient bone marrow–derived macrophages responded to IAV infection with enhanced activation of caspase-1 relative to wild-type macrophages (**Supplementary Fig. 4f**). To confirm the role of autophagy in *Ripk2*$^{-/-}$ cells, we treated *Ripk2*$^{-/-}$ BMDCs with rapamycin to force the induction of autophagy. After treatment with rapamycin, IL-18 production and caspase-1 activation in *Ripk2*$^{-/-}$ BMDCs diminished to wild-type amounts (**Fig. 6d**,**e**). We next verified the role of autophagy *in vivo* and found that the amount of LC3-II protein was lower in the lungs of IAV-infected *Ripk2*$^{-/-}$ mice relative to WT controls (**Fig. 6f**). We also examined the effects of inducing autophagy *in vivo* with rapamycin treatment in IAV-infected *Ripk2*$^{-/-}$ mice and observed that rapamycin treatment dampened recruitment of neutrophils and production of inflammatory cytokines in *Ripk2*$^{-/-}$ mice (**Fig. 6g**,**h**). Together, these results demonstrate that RIPK2 negatively regulates inflammasome activation, inflammatory cytokine production and neutrophil recruitment by inducing autophagy in IAV-infected cells and mice.

Viral RNA genomes activate autophagy through NOD2-RIPK2

To examine the mechanism by which NOD2 and RIPK2 induce autophagy, we expressed RIPK2 and NOD2 in the presence or absence of IAV infection and determined that infection induced an interaction between RIPK2 and NOD2 (**Supplementary Fig. 5a**). Next, we determined the viral ligand that triggers NOD2-RIPK2 signaling. The cytosolic delivery of viral RNA analogs (polyribo-inosinic:polyribocytidylic acid (poly (I:C)) plus the transfection reagent LyoVec) induced LC3-II conversion in a RIPK2-dependent and NOD2-dependent manner (**Supplementary Fig. 5b**). However, extracellular delivery of naked poly(I:C) induced LC3-II conversion independently of the RIPK2 pathway (**Supplementary Fig. 5c**). We also transfected BMDCs with purified viral RNA genomes and determined that IAV viral RNA induces autophagy in a RIPK2-dependent manner (**Supplementary Fig. 5d**). Finally, transfection of IAV viral RNA followed by treatment with ATP resulted in enhanced production of IL-18 in both *Ripk2*$^{-/-}$ and *Nod2*$^{-/-}$ BMDCs (**Supplementary Fig. 5e**). These data indicate that cytosolic viral genomes activate the cytosolic NOD2-RIPK2 signaling pathway to trigger autophagy.

NOD2-RIPK2–mediated mitophagy regulates the inflammasome

In addition to preserving cellular energy stores, autophagy is linked to the removal of damaged mitochondria. Notably, mitochondrial damage and the subsequent release of reactive oxygen species (ROS) is linked to activation of the NLRP3 inflammasome[34,37]. We thus hypothesized that defective mitophagy induction in IAV-infected RIPK2-deficient cells triggered greater inflammasome activation because of the accumulation of damaged mitochondria. To investigate this possibility, we examined mitochondrial superoxide production after IAV infection. IAV infection increased the production of mitochondrial superoxide in *Ripk2*$^{-/-}$ and *Nod2*$^{-/-}$ BMDCs to a markedly greater extent than in wild-type BMDCs (**Fig. 7a** and

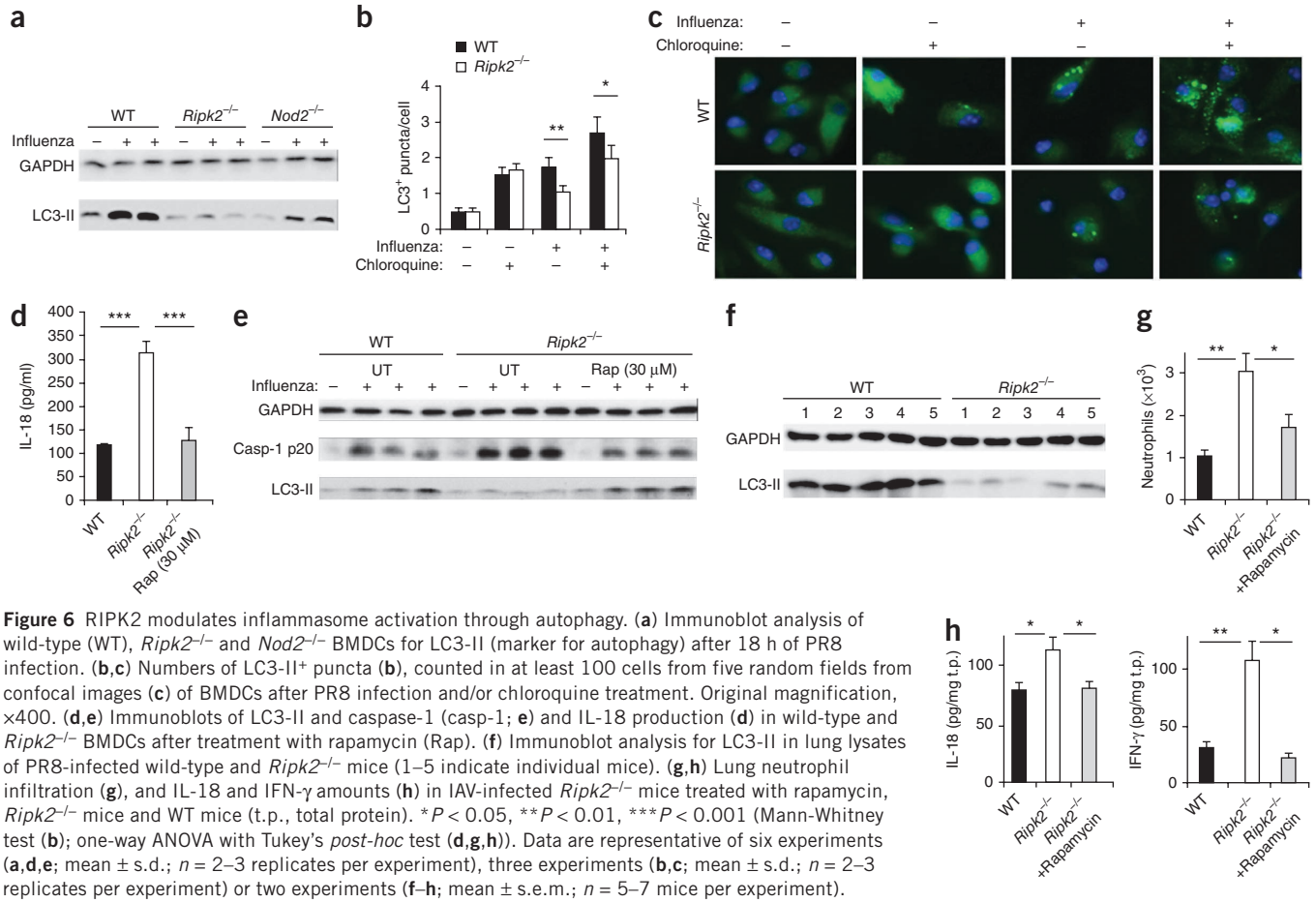

Figure 6 RIPK2 modulates inflammasome activation through autophagy. (**a**) Immunoblot analysis of wild-type (WT), *Ripk2*$^{-/-}$ and *Nod2*$^{-/-}$ BMDCs for LC3-II (marker for autophagy) after 18 h of PR8 infection. (**b**,**c**) Numbers of LC3-II^{+} puncta (**b**), counted in at least 100 cells from five random fields from confocal images (**c**) of BMDCs after PR8 infection and/or chloroquine treatment. Original magnification, ×400. (**d**,**e**) Immunoblots of LC3-II and caspase-1 (casp-1; **e**) and IL-18 production (**d**) in wild-type and *Ripk2*$^{-/-}$ BMDCs after treatment with rapamycin (Rap). (**f**) Immunoblot analysis for LC3-II in lung lysates of PR8-infected wild-type and *Ripk2*$^{-/-}$ mice (1–5 indicate individual mice). (**g**,**h**) Lung neutrophil infiltration (**g**), and IL-18 and IFN-γ amounts (**h**) in IAV-infected *Ripk2*$^{-/-}$ mice treated with rapamycin, *Ripk2*$^{-/-}$ mice and WT mice (t.p., total protein). $^{*}P < 0.05$, $^{**}P < 0.01$, $^{***}P < 0.001$ (Mann-Whitney test (**b**); one-way ANOVA with Tukey's *post-hoc* test (**d**,**g**,**h**)). Data are representative of six experiments (**a**,**d**,**e**; mean ± s.d.; $n = 2$–3 replicates per experiment), three experiments (**b**,**c**; mean ± s.d.; $n = 2$–3 replicates per experiment) or two experiments (**f**–**h**; mean ± s.e.m.; $n = 5$–7 mice per experiment).

Supplementary Fig. 6a,**b**). To confirm that mitochondrial damage was responsible for our observed phenotype, we examined mitochondrial superoxide during *Listeria* infection. Although *Listeria* infection generated a more robust production of superoxide compared to IAV infection, there was no difference between wild-type and *Ripk2*$^{-/-}$ cells (**Fig. 7b** and **Supplementary Fig. 6c**). We also counted damaged mitochondria (disrupted cristae) using electron microscopy and determined that IAV-infected *Ripk2*$^{-/-}$ BMDCs had a greater ratio of damaged to healthy mitochondria than did wild-type controls (**Supplementary Fig. 6d**). We confirmed the role of mitophagy in our model by staining BMDCs infected with IAV or *Listeria* with MitoTracker Green and examined the fluorescence intensity by flow cytometry. Cells with higher geometric mean fluorescence intensity (MFI) indicate an accumulation of mitochondria. Although *Ripk2*$^{-/-}$ cells in some experiments had more mitochondria even before infection, we observed that IAV-infected *Ripk2*$^{-/-}$ BMDCs, but not wild-type ones, exhibited an increase in the number of mitochondria, and we did not observe this increase in *Listeria*-infected *Ripk2*$^{-/-}$ cells (**Fig. 7c** and **Supplementary Fig. 7a–c**). We confirmed these findings by isolating DNA from BMDCs and comparing the ratio of nuclear DNA to mitochondrial DNA. Using this approach, we also determined that there were more mitochondria in IAV-infected *Ripk2*$^{-/-}$ BMDCs compared to wild-type BMDCs (**Supplementary Fig. 7d**). As mitophagy appears to be defective in *Ripk2*$^{-/-}$ cells, resulting in greater production of mitochondrial superoxide, we treated *Ripk2*$^{-/-}$ BMDCs with *N*-acetyl cysteine (NAC), a general ROS inhibitor, and found significantly less IL-18 and caspase-1 activation relative to control-treated *Ripk2*$^{-/-}$ BMDCs infected with IAV **(Fig. 7d**,**e)**. We obtained similar results with the specific mitochondrial superoxide inhibitor mitoTEMPO **(Fig. 7f)**. To confirm the specificity of these results, we treated *Ripk2*$^{-/-}$*Listeria*-infected BMDCs with NAC. In agreement with the role for the AIM2 inflammasome in *Listeria* infection, we observed little or no effect of NAC treatment during *Listeria* infection (**Supplementary Fig. 7e**). Finally, we verified directly that mitophagy was lower during IAV infection in *Ripk2*$^{-/-}$ BMDCs compared to infected wild-type cells by staining for LC3 and mitochondria. The ratio of LC3^{+} puncta that localized with mitochondria, as assayed by confocal microscopy, was significantly lower in *Ripk2*$^{-/-}$ cells compared to wild-type BMDCs (**Fig. 7g**). These results indicate that the induction of mitophagy during IAV infection, which is regulated by NOD2 and RIPK2, is essential for the clearance of damaged mitochondria. In the absence of RIPK2 or NOD2, elevated production of mitochondrial superoxide enhanced activation of the NLRP3 inflammasome.

RIPK2 regulates mitophagy through its kinase activity

RIPK2 has been reported to regulate autophagy through the autophagy protein ATG16L1 (refs. 22,23). However, another group found no interaction between RIPK2 and ATG16L1 (ref. 37). To examine how RIPK2 regulates mitophagy during viral infection, we first examined the possibility that RIPK2 might interact with ATG16L1. We expressed RIPK2 and the autophagy-related protein ATG16L1 in the presence or absence of NOD2 and IAV infection. IAV infection was required for association of RIPK2, NOD2 and ATG16L1 (**Supplementary Fig. 8a**). However, endogenous RIPK2 did not immunoprecipitate with ATG16L1, and we did not detect substantial colocalization of these

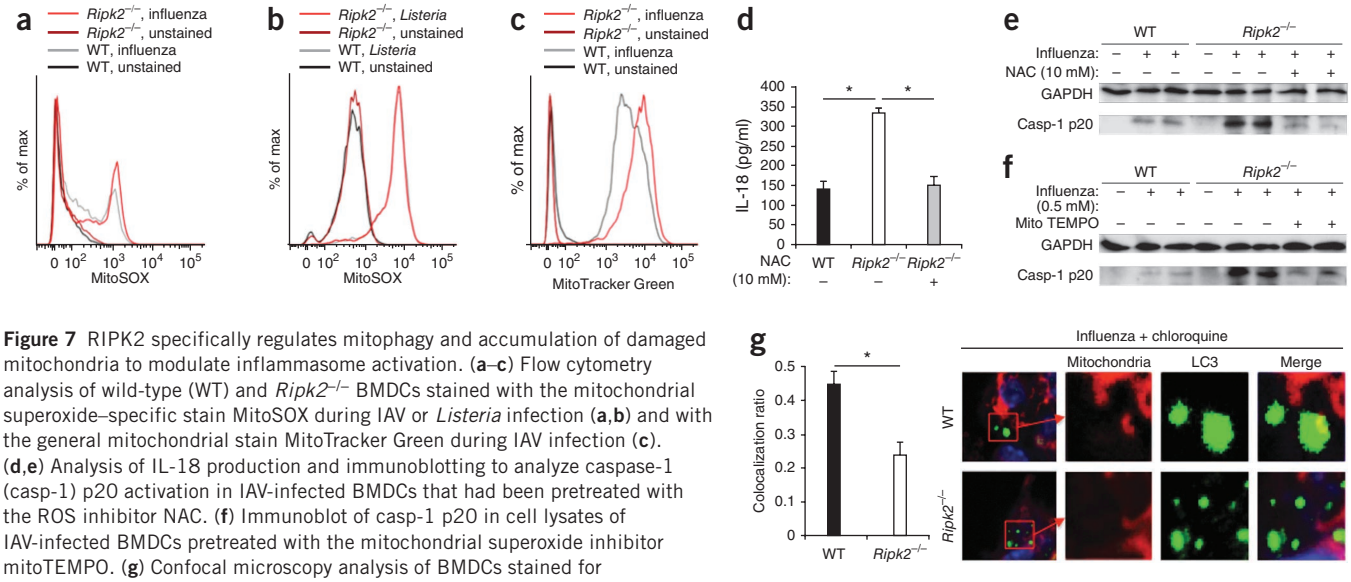

Figure 7 RIPK2 specifically regulates mitophagy and accumulation of damaged mitochondria to modulate inflammasome activation. (**a**–**c**) Flow cytometry analysis of wild-type (WT) and *Ripk2*$^{-/-}$ BMDCs stained with the mitochondrial superoxide–specific stain MitoSOX during IAV or *Listeria* infection (**a**,**b**) and with the general mitochondrial stain MitoTracker Green during IAV infection (**c**). (**d**,**e**) Analysis of IL-18 production and immunoblotting to analyze caspase-1 (casp-1) p20 activation in IAV-infected BMDCs that had been pretreated with the ROS inhibitor NAC. (**f**) Immunoblot of casp-1 p20 in cell lysates of IAV-infected BMDCs pretreated with the mitochondrial superoxide inhibitor mitoTEMPO. (**g**) Confocal microscopy analysis of BMDCs stained for mitochondria (red) and LC3 (green) for colocalization as an indicator of mitophagy. Original magnification, ×400; inset (red boxed region) was digitally enlarged ×10. *$P < 0.01$ (one-way ANOVA with Tukey's *post-hoc* test (**d**) and unpaired two-sided Student's *t*-test (**g**)). Data are representative of nine experiments (**a**), three experiments (**b**,**d**–**g**) or six experiments (**c**) (mean ± s.d.; $n = 2$–3 replicates per experiment).

proteins by immunofluorescence confocal microscopy in BMDCs during IAV infection (data not shown). Although the overexpression data above suggest that the interaction with ATG16L1 may be important during IAV infection, this remains to be verified under endogenous conditions. Furthermore, an interaction between RIPK2 and ATG16L1 still does not address the upstream signaling that initiates mitophagy during infection. To begin to address the exact mechanism by which RIPK2 regulates mitophagy in our model, we examined the role of RIPK2's kinase activity during induction of mitophagy. Treatment of wild-type BMDCs with the p38 and RIPK2 inhibitor SB203580 resulted in less LC3-II conversion and more caspase-1 activation as well as greater IL-18 production (**Fig. 8a**,**b**). We confirmed that this effect was due to inhibition of RIPK2 by examining autophagy in p38-deficient BMDCs. p38 deficiency did not impact LC3-II conversion during IAV infection, indicating that the effect of SB203580 was mediated by inhibition of RIPK2 (**Supplementary Fig. 8b**). Next, we examined autophagy proteins known to be activated by phosphorylation and discovered that the extent of phosphorylation of ULK1 at Ser555 was less in *Ripk2*$^{-/-}$ BMDCs during IAV infection, although upregulation of total ULK1 was not affected (**Fig. 8c**). Phosphorylation at Ser555 of ULK1 is known to be important for its activation, and ULK1 is known to have an important role in mitophagy, especially during hematopoietic development[38]. We therefore examined *Ulk1*$^{-/-}$ BMDCs and found that they also have increased

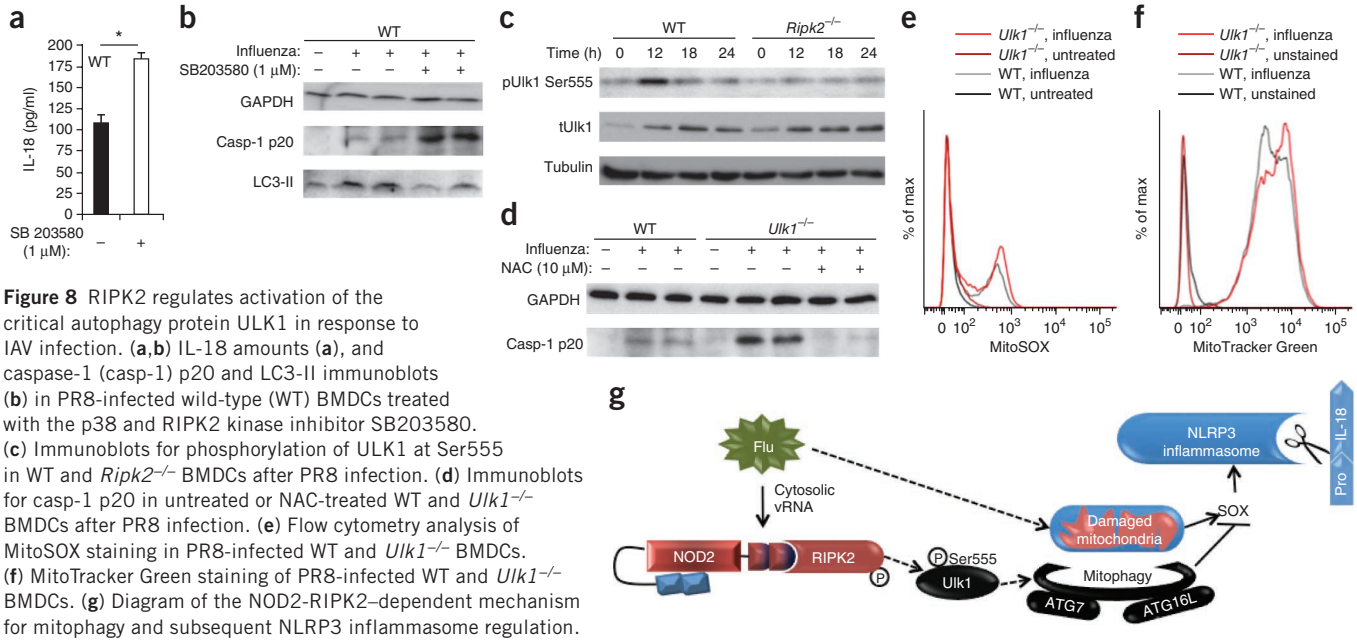

Figure 8 RIPK2 regulates activation of the critical autophagy protein ULK1 in response to IAV infection. (**a**,**b**) IL-18 amounts (**a**), and caspase-1 (casp-1) p20 and LC3-II immunoblots (**b**) in PR8-infected wild-type (WT) BMDCs treated with the p38 and RIPK2 kinase inhibitor SB203580. (**c**) Immunoblots for phosphorylation of ULK1 at Ser555 in WT and *Ripk2*$^{-/-}$ BMDCs after PR8 infection. (**d**) Immunoblots for casp-1 p20 in untreated or NAC-treated WT and *Ulk1*$^{-/-}$ BMDCs after PR8 infection. (**e**) Flow cytometry analysis of MitoSOX staining in PR8-infected WT and *Ulk1*$^{-/-}$ BMDCs. (**f**) MitoTracker Green staining of PR8-infected WT and *Ulk1*$^{-/-}$ BMDCs. (**g**) Diagram of the NOD2-RIPK2–dependent mechanism for mitophagy and subsequent NLRP3 inflammasome regulation. *$P < 0.05$ (unpaired two-sided Student's *t*-test). Data are representative of three experiments (**a**–**c**) or two experiments (**d**–**f**) (mean ± s.d.; $n = 2$–3 replicates per experiment).

activation of caspase-1 after infection with IAV and this increased activation of caspase-1 was suppressed by NAC treatment (**Fig. 8d**). Furthermore, *Ulk1*$^{-/-}$ BMDCs had more mitochondrial damage and greater mitochondrial mass compared to wild-type BMDCs (**Fig. 8e**,**f** and **Supplementary Fig. 8c**). Collectively, these data demonstrate that NOD2 and RIPK2 interact with each other in response to IAV RNA genomes and regulate mitophagy in a manner dependent on the kinase activity of RIPK2 and on ULK1. Mitophagy is then responsible for removing damaged mitochondria and preventing excessive activation of NLRP3 and production of IL-18 (**Fig. 8g**).

DISCUSSION

Although the *in vivo* relevance of RIPK2-mediated signaling for immunity against bacterial pathogens has been clearly demonstrated for pathogens such as *Helicobacter pylori* and *Listeria monocytogenes*[39,40], the role of RIPK2 in the immune response to viral infections *in vivo* has not been reported to our knowledge. In addition, the involvement of RIPK2 in signaling pathways other than the regulation of NF-κB and MAP kinase has not been explored in detail.

Here we demonstrated that RIPK2 is critical for protection against IAV-induced immunopathology during IAV infection. Our results demonstrate that RIPK2 functions by negatively regulating production of IL-18 and IFN-γ in stromal and immune cells of the pulmonary tract. We identified NOD2 as the NLR acting upstream of RIPK2 in mediating protection against IAV-induced morbidity and mortality. These results thus implicate NOD2 as a key partner in additional immune signaling pathways during viral infection, beyond those previously discovered for type I interferons[25,26].

Although we observed elevated IL-1β *in vitro* by infecting BMDCs with IAV, the amount of IL-1β present *in vivo* was 5–10 times lower than that of IL-18. These low amounts of IL-1β *in vivo* likely obscured our ability to detect differences in this cytokine initially. We expect that IL-1β may also have some role in our model *in vivo*; however, we illustrated the importance of RIPK2-mediated dampening of IL-18 by the marked effect of IL-18–neutralizing antibodies in reducing the morbidity and mortality in *Ripk2*-deficient mice infected with IAV, and we confirmed this in *Ripk2*$^{-/-}$*Il18*$^{-/-}$ mice. This demonstrates that excessive IL-18 production in *Ripk2*$^{-/-}$ mice drives the majority of the immunopathology.

Immunopathology is a key factor in acute fatal IAV pneumonia in humans and in animal models infected with highly virulent IAV strains[41,42]. Our finding that IL-18 mediates hyperinflammatory responses in *Ripk2*$^{-/-}$ mice thus opens new possibilities for the treatment of severe IAV infections. In other disease models, elevated IL-18 has been shown to promote neutrophil infiltration, and to mediate the production of IFN-γ and chemokines (lipopolysaccharide-induced toxemia and ischemic reperfusion, respectively). Decreasing the amount of IL-18 in these experimental systems limits the extent of tissue damage and promotes survival[43,44]. Blocking IL-18 may limit the extent of lung immunopathology in situations where IAV infection leads to extreme respiratory distress.

At the molecular level, our data show that RIPK2 dampens harmful IL-18–driven inflammatory responses against IAV by preventing excessive activation of caspase-1 through a mitophagy-mediated suppression mechanism rather than via a direct interaction with caspase-1. Multiple inflammasomes that activate caspase-1 in a pathogen-dependent manner have been identified. However, our previous studies had identified a critical role for the NLRP3 inflammasome in regulating production of IL-1β and IL-18 in IAV infection both *in vivo* and *in vitro*[12,13]. Here we extended these findings by showing that RIPK2-mediated inhibition of inflammasome activation proceeds through the removal of damaged mitochondria and subsequently lower mitochondrial production of superoxide, a known activator of the NLRP3 inflammasome[35,45]. We verified the role of the NLRP3 inflammasome in our model by treatment with the NLRP3-specific inhibitor glyburide.

Many reports differ on the mechanism by which RIPK2 regulates the induction of autophagy or xenophagy in response to bacterial infection[20,22,23,37]. In fact, there are differing reports on the role of RIPK2 and ATG16L1 during bacterial infection[22,23,37]. Although we observed an interaction between these two proteins when they were overexpressed, we could not verify this interaction in BMDCs during IAV infection, despite the use of multiple methods and conditions. We therefore sought out other potential mechanisms by which RIPK2 could regulate autophagy. We discovered that *Ripk2*$^{-/-}$ BMDCs had more mitochondrial damage and more mitochondrial mass, suggesting that mitophagy was defective. To identify the mechanisms involved in RIPK2-mediated mitophagy, we examined the mitophagy protein Parkin through the use of Parkin-deficient mice (*Park2*$^{-/-}$). However, we did not observe any role for Parkin in our model (data not shown). In the end, we discovered that activation of ULK1 by phosphorylation at Ser555 was less in *Ripk2*$^{-/-}$ BMDCs compared to wild-type controls. We also verified the importance of ULK1 in our model as *Ulk1*$^{-/-}$ BMDCs phenocopied *Ripk2*$^{-/-}$ BMDCs with regard to mitochondrial damage and inflammasome activation. Our findings highlight a signaling pathway in which NOD2 and RIPK2 respond to viral infection by promoting ULK1 phosphorylation and inducing mitophagic responses that dampen inflammasome activation and IL-18 production. Although it is clear that Ripk2 deficiency resulted in less ULK1 phosphorylation, it is not clear whether RIPK2 directly phosphorylates ULK1 or whether there are other intermediates that are regulated by RIPK2, which subsequently activate ULK1.

Recently, autophagy has been shown to directly clear inflammasomes from activated cells, thus modulating inflammation[17]. However, we did not observe any role for autophagy in our system during *Listeria* infection dependent on the AIM2 inflammasome, suggesting that global degradation of the inflammasome by macroautophagy is likely not important in our model. Furthermore, virus replication was not affected in our model, suggesting that xenophagy also does not have a substantial role. Therefore, our data are the first to our knowledge to demonstrate that NOD2-RIPK2 signaling can regulate mitophagy specifically during viral infection and to demonstrate the physiological relevance of this pathway in controlling pulmonary inflammation *in vivo*. Notably, *Rikp2*$^{-/-}$ cells had slightly higher basal mitochondrial mass and numbers of damaged mitochondria. These data may indicate a role for Ripk2 in the steady-state regulation of mitophagy. In the future it will be of interest to examine whether this can exacerbate other non-infectious diseases where mitochondrial damage or metabolic stresses are known to be factors. In all, our findings demonstrate that NOD2-RIPK2 signaling is involved in the recognition of a wider variety of pathogens than previously thought, and we determined that RIPK2 can regulate ULK1 mediated mitophagy. Finally, our results provide a unifying principle by linking NOD2-RIPK2 signaling, autophagy or mitophagy, and inflammasome–IL-18 production together, suggesting that this pathway is a critical regulatory mechanism for preventing overt inflammation under certain disease conditions.

METHODS

Methods and any associated references are available in the online version of the paper.

Note: Supplementary information is available in the online version of the paper.

ACKNOWLEDGMENTS

We thank members of the Veterinary Pathology Core lab at St. Jude for their work in processing of hematoxylin and eosin–stained and immunohistochemistry slides, members of the Cell and Tissue Imaging Core facility for their help in preparing and imaging transmission electron microscopy samples, and A. Coyle, E. Grant, J. Bertin (Millennium Pharmaceuticals), T. Mak (University of Toronto) and R. Flavell (Yale University) for providing mutant mice. M.L. is supported by grants from the EU Framework Program 7 (Marie-Curie grant 256432), European Research Council (grant 281600) and the Fund for Scientific Research Flanders (G030212N, 1.2.201.10.N.00 and 1.5.122.11.N.00). This work was supported by US National Institutes of Health grants (AR056296, AI101935 and CA163507) and the American Lebanese Syrian Associated Charities to T.-D.K.

AUTHOR CONTRIBUTIONS

C.L. designed and conducted experiments, and wrote the manuscript. P.G.T. helped conduct the initial experiments *in vivo* in *Ripk2*$^{-/-}$ mice and helped design T cell experiments. P.K.A. conducted experiments with *L. monocytogenes* and helped write the manuscript. P.V. helped design experiments and interpret histopathology data. S.M. helped design and conduct experiments related to mitophagy and mitochondrial damage. J.M. helped design experiments related to mitophagy and mitochondrial damage. G.H. helped design and conduct experiments with *Mapk14* conditional knockout mice. M.G. conducted experiments for IL-18, NF-κB and MAPK signaling. M.K. helped design experiments, and provided *Ulk1*$^{-/-}$ mice and other reagents for ULK1 experiments. H.C. helped design experiments and provided *Mapk14* conditional knockout mice. R.J.X. helped design experiments and provided reagents for ATG16-related experiments and autophagy in general. D.R.G. helped design experiments and provided reagents for mitophagy-related experiments. M.L. helped design experiments and provided reagents for caspase-1 activation and interaction studies. C.A.D. helped design experiments and provided reagents for IL-18 neutralization studies. P.C.D. helped design experiments, provided reagents for T cell experiments and helped write the manuscript. T.-D.K. conceived project, designed experiments, analyzed data, helped write the manuscript and oversaw the project.

COMPETING FINANCIAL INTERESTS

The authors declare no competing financial interests.

1. Kilbourne, E.D. Influenza pandemics of the 20th century. *Emerg. Infect. Dis.* **12**, 9–14 (2006).
2. Taubenberger, J.K. & Morens, D.M. 1918 Influenza: the mother of all pandemics. *Emerg. Infect. Dis.* **12**, 15–22 (2006).
3. de Jong, M.D. *et al.* Fatal outcome of human influenza A (H5N1) is associated with high viral load and hypercytokinemia. *Nat. Med.* **12**, 1203–1207 (2006).
4. Kobasa, D. *et al.* Aberrant innate immune response in lethal infection of macaques with the 1918 influenza virus. *Nature* **445**, 319–323 (2007).
5. Perrone, L.A., Plowden, J.K., Garcia-Sastre, A., Katz, J.M. & Tumpey, T.M. H5N1 and 1918 pandemic influenza virus infection results in early and excessive infiltration of macrophages and neutrophils in the lungs of mice. *PLoS Pathog.* **4**, e1000115 (2008).
6. Tumpey, T.M. *et al.* Characterization of the reconstructed 1918 Spanish influenza pandemic virus. *Science* **310**, 77–80 (2005).
7. Guillot, L. *et al.* Involvement of toll-like receptor 3 in the immune response of lung epithelial cells to double-stranded RNA and influenza A virus. *J. Biol. Chem.* **280**, 5571–5580 (2005).
8. Heer, A.K. *et al.* TLR signaling fine-tunes anti-influenza B cell responses without regulating effector T cell responses. *J. Immunol.* **178**, 2182–2191 (2007).
9. Rehwinkel, J. *et al.* RIG-I detects viral genomic RNA during negative-strand RNA virus infection. *Cell* **140**, 397–408 (2010).
10. Allen, I.C. *et al.* The NLRP3 inflammasome mediates in vivo innate immunity to influenza A virus through recognition of viral RNA. *Immunity* **30**, 556–565 (2009).
11. Ichinohe, T., Pang, I.K. & Iwasaki, A. Influenza virus activates inflammasomes via its intracellular M2 ion channel. *Nat. Immunol.* **11**, 404–410 (2010).
12. Thomas, P.G. *et al.* The intracellular sensor NLRP3 mediates key innate and healing responses to influenza A virus via the regulation of caspase-1. *Immunity* **30**, 566–575 (2009).
13. Kanneganti, T.D. *et al.* Critical role for Cryopyrin/Nalp3 in activation of caspase-1 in response to viral infection and double-stranded RNA. *J. Biol. Chem.* **281**, 36560–36568 (2006).
14. Martinon, F., Burns, K. & Tschopp, J. The inflammasome: a molecular platform triggering activation of inflammatory caspases and processing of proIL-beta. *Mol. Cell* **10**, 417–426 (2002).
15. Schroder, K. & Tschopp, J. The inflammasomes. *Cell* **140**, 821–832 (2010).
16. Mortimore, G.E., Hutson, N.J. & Surmacz, C.A. Quantitative correlation between proteolysis and macro- and microautophagy in mouse hepatocytes during starvation and refeeding. *Proc. Natl. Acad. Sci. USA* **80**, 2179–2183 (1983).
17. Shi, C.S. *et al.* Activation of autophagy by inflammatory signals limits IL-1beta production by targeting ubiquitinated inflammasomes for destruction. *Nat. Immunol.* **13**, 255–263 (2012).
18. Geisler, S. *et al.* The PINK1/Parkin-mediated mitophagy is compromised by PD-associated mutations. *Autophagy* **6**, 871–878 (2010).
19. Sandoval, H. *et al.* Essential role for Nix in autophagic maturation of erythroid cells. *Nature* **454**, 232–235 (2008).
20. Anand, P.K. *et al.* TLR2 and RIP2 pathways mediate autophagy of Listeria monocytogenes via extracellular signal-regulated kinase (ERK) activation. *J. Biol. Chem.* **286**, 42981–42991 (2011).
21. Uhl, M. *et al.* Autophagy within the antigen donor cell facilitates efficient antigen cross-priming of virus-specific CD8+ T cells. *Cell Death Differ.* **16**, 991–1005 (2009).
22. Cooney, R. *et al.* NOD2 stimulation induces autophagy in dendritic cells influencing bacterial handling and antigen presentation. *Nat. Med.* **16**, 90–97 (2010).
23. Homer, C.R., Richmond, A.L., Rebert, N.A., Achkar, J.P. & McDonald, C. ATG16L1 and NOD2 interact in an autophagy-dependent antibacterial pathway implicated in Crohn's disease pathogenesis. *Gastroenterology* **139**, 1630–1641 (2010).
24. Kobayashi, K. *et al.* RICK/Rip2/CARDIAK mediates signalling for receptors of the innate and adaptive immune systems. *Nature* **416**, 194–199 (2002).
25. Dugan, J.W. *et al.* Nucleotide oligomerization domain-2 interacts with 2′-5′-oligoadenylate synthetase type 2 and enhances RNase-L function in THP-1 cells. *Mol. Immunol.* **47**, 560–566 (2009).
26. Sabbah, A. *et al.* Activation of innate immune antiviral responses by Nod2. *Nat. Immunol.* **10**, 1073–1080 (2009).
27. Park, J.H. *et al.* RICK/RIP2 mediates innate immune responses induced through Nod1 and Nod2 but not TLRs. *J. Immunol.* **178**, 2380–2386 (2007).
28. Ishikawa, H. *et al.* IFN-gamma production downstream of NKT cell activation in mice infected with influenza virus enhances the cytolytic activities of both NK cells and viral antigen-specific CD8+ T cells. *Virology* **407**, 325–332 (2010).
29. Okamura, H. *et al.* Cloning of a new cytokine that induces IFN-gamma production by T cells. *Nature* **378**, 88–91 (1995).
30. Kim, S. *et al.* Listeria monocytogenes is sensed by the NLRP3 and AIM2 inflammasome. *Eur. J. Immunol.* **40**, 1545–1551 (2010).
31. Black, R.A., Kronheim, S.R., Merriam, J.E., March, C.J. & Hopp, T.P. A pre-aspartate-specific protease from human leukocytes that cleaves pro-interleukin-1 beta. *J. Biol. Chem.* **264**, 5323–5326 (1989).
32. Lamkanfi, M. *et al.* Glyburide inhibits the Cryopyrin/Nalp3 inflammasome. *J. Cell Biol.* **187**, 61–70 (2009).
33. Tsuchiya, K. *et al.* Involvement of absent in melanoma 2 in inflammasome activation in macrophages infected with Listeria monocytogenes. *J. Immunol.* **185**, 1186–1195 (2010).
34. Sarkar, A. *et al.* ASC directs NF-kappaB activation by regulating receptor interacting protein-2 (RIP2) caspase-1 interactions. *J. Immunol.* **176**, 4979–4986 (2006).
35. Nakahira, K. *et al.* Autophagy proteins regulate innate immune responses by inhibiting the release of mitochondrial DNA mediated by the NALP3 inflammasome. *Nat. Immunol.* **12**, 222–230 (2011).
36. Saitoh, T. *et al.* Loss of the autophagy protein Atg16L1 enhances endotoxin-induced IL-1beta production. *Nature* **456**, 264–268 (2008).
37. Travassos, L.H. *et al.* Nod1 and Nod2 direct autophagy by recruiting ATG16L1 to the plasma membrane at the site of bacterial entry. *Nat. Immunol.* **11**, 55–62 (2010).
38. Joo, J.H. *et al.* Hsp90-Cdc37 chaperone complex regulates Ulk1- and Atg13-mediated mitophagy. *Mol. Cell* **43**, 572–585 (2011).
39. Viala, J. *et al.* Nod1 responds to peptidoglycan delivered by the *Helicobacter pylori* cag pathogenicity island. *Nat. Immunol.* **5**, 1166–1174 (2004).
40. Kobayashi, K.S. *et al.* Nod2-dependent regulation of innate and adaptive immunity in the intestinal tract. *Science* **307**, 731–734 (2005).
41. Kash, J.C. *et al.* Genomic analysis of increased host immune and cell death responses induced by 1918 influenza virus. *Nature* **443**, 578–581 (2006).
42. Rainsford, K.D. Influenza ("Bird Flu"), inflammation and anti-inflammatory/analgesic drugs. *Inflammopharmacology* **14**, 2–9 (2006).
43. Netea, M.G. *et al.* Neutralization of IL-18 reduces neutrophil tissue accumulation and protects mice against lethal *Escherichia coli* and *Salmonella typhimurium* endotoxemia. *J. Immunol.* **164**, 2644–2649 (2000).
44. Raeburn, C.D. *et al.* Neutralization of IL-18 attenuates lipopolysaccharide-induced myocardial dysfunction. *Am. J. Physiol. Heart Circ. Physiol.* **283**, H650–H657 (2002).
45. Zhou, R., Yazdi, A.S., Menu, P. & Tschopp, J. A role for mitochondria in NLRP3 inflammasome activation. *Nature* **469**, 221–225 (2011).

ONLINE METHODS

Virus, bacteria and ligands. The influenza A/Puerto Rico/8/34 H1N1 virus (PR8) was generated by an eight-plasmid reverse genetics system[46]. X31 virus was prepared similarly. Stocks were propagated no more than twice by allantoic inoculation of 10-d-old embryonated hen's eggs with seed virus diluted 1:10^4. *L. monocytogenes* was grown in brain-heart infusion medium at 37 °C overnight and then subcultured to mid-log phase for infections. Poly(I:C) and poly(I:C) LyoVec (Invivogen) were used at the concentrations indicated in each figure. IAV genomes, or cellular mRNA controls, were purified from viral stocks or BMDCs using Trizol LS and transfected using Lipofectamine 2000 according to manufacturer's instructions (Invitrogen).

Measuring virus titers. Near-confluent 9.6 cm^2 monolayers of Madin-Darby canine kidney (MDCK) cells were infected with 1-ml aliquots of tenfold dilutions (10^3–10^5) of lung homogenate, washed and overlayed with 3 ml minimum essential medium (MEM) containing 1 mg/ml L-1-tosylamido-2-phenylethyl chloromethyl ketone-treated trypsin (Sigma-Aldrich) and 1.0% Sea Plaque agarose (Lonza). After 3 d, plaques were visualized with crystal violet (Alfa Aesar).

Mice. All mice were maintained at St. Jude Children's Research Hospital and were fully on the C57BL/6J (B6) background. *Nod2*$^{-/-}$, LysM-Cre^{+} *Atg7*$^{loxP/loxP}$ GFP-LC3^{+} (flanking *loxP* sites allow for Cre recombinase–mediated deletion of the *Atg7* gene), p38$^{loxP/loxP}$ (*Mapk14*$^{loxP/loxP}$ Rosa26-Cre-ER^{T2}), *Ulk1*$^{-/-}$ and *Ripk2*$^{-/-}$ (refs. 24,32,40,47–49) mice have been reported previously, and *Ripk2*$^{-/-}$ × *Il-18*$^{-/-}$ double-deficient mice were generated by backcrossing. All mice were housed in a specific pathogen–free (SPF) facility, and experiments were conducted under protocols approved by the St. Jude Children's Research Hospital Committee on Use and Care of Animals.

Virus infection and sampling. Mice were anesthetized with 2,2,2-tribromoethanol (Avertin, Sigma-Aldrich) and infected intranasally with the indicated dose of the PR8 virus in 30 µl of endotoxin-free PBS. In the case of IL-18 neutralization, mice were injected as indicated with 200 µl of rabbit antiserum to mouse IL-18. For *in vivo* induction of autophagy, mice were injected with 600 µg/kg of rapamycin on days 0, 1 and 2, and samples were collected 6 h after the final injection. Mice were either weighed and monitored for severe illness daily for 14–16 d, or whole lungs were collected from mice at various intervals for analysis. The right lungs were processed by mincing and passing through a 70-µm cell strainer using a total of 4 ml Hank's balanced salt solution (HBSS). After low speed centrifugation, total cell numbers per lung or lymph node were determined, and cells were stained for flow cytometry. In addition, HBSS supernatant was used for virus titration and cytokine analysis. The left lungs were used for histopathological analysis or ground in RIPA buffer with protease inhibitor and phosphatase inhibitor (Calbiochem) followed by boiling in SDS sample buffer and examination by immunoblot.

Flow cytometry. Aliquots of whole lung populations (as above) were stained for myeloid cells with anti-CD11b, anti-MHC Class II, anti-GR1 and anti-CD11c (Biolegend, M1/70, M5/114.15.2, RB6-8C5 and N418, respectively) monoclonal antibodies, and annexin V after blocking the Fc receptor with anti-CD32/CD16 antibody (Biolegend, Truestain fcX, 101320) at 4 °C and analyzed by flow cytometry (macrophages: CD11b^{+}, CD11c^{-}, GR1$^{-,lo}$; granulocytes, CD11b^{hi}, CD11c^{-}, GR1^{hi}; DCs: CD11c^{+}, MHC class II^{+}). Additionally, lymphocytes were stained with anti-CD19, anti-TCRβ, anti-CD8 and anti-CD4 (Biolegend, 6D5, H57-597, 53-6.7 and RM4-5, respectively). NK and NKT cells were stained with anti-CD3 and anti-NK1.1 (Biolegend, 145-2C11 and PK136). For NK, NKT and CD8^{+} T cell activation experiments, anti-CD3 and anti-NK1.1 or anti-TCRβ, anti-CD8 and anti-CD44 (Biolegend, IM7) markers were used. Intracellular IFN-γ (Biolegend, XMG1.2) in CD8^{+} T cells was measured after stimulation of whole lung cells for 5 h at 37 °C and 5% CO_2 with a cocktail of IAV peptides (PB1, PB1-F2, NP, PA, M1) at 1 µg/ml each with monensin. NK and NKT cells were similarly restimulated with 10 ng/ml IL-12. Cell numbers represent one-tenth of the total number present in the right lung lobes.

For staining mitochondria, BMDCs were uninfected as controls or infected for 6 h with a multiplicity of infection (MOI) of 10 *Listeria* or 18–24 h with MOI of 10 PR8 influenza and then stained for 30 min in fresh complete RPMI-1640 medium containing 5 µM MitoSOX or 2 µM MitoTracker Green. Cells were then washed in HBSS, resuspended in flow cytometry buffer (DPBS with 1% FBS and 0.04% NaN_3) and analyzed immediately by flow cytometry.

Assaying for cytokines and chemokines. Mouse cytokines and chemokines in HBSS supernatants from whole lung homogenates were measured using the Millipore 22-multiplex assay following the manufacturer's instructions. In addition, lung samples and supernatants from BMDCs cultured *in vitro* were assayed by ELISA for IL-18 (MBL International) and IL-1β or IFN-γ (eBiosciences). All cytokines from lung homogenates were normalized to the total protein in the homogenate by BCA protein assay (Pierce) and expressed as cytokine concentration per milligram total protein.

Histopathological analysis, transmission electron microscopy and confocal microscopy. Formalin-preserved left lungs were embedded in paraffin and processed by standard techniques. Longitudinal 5-µm sections were stained with hematoxylin and eosin, and examined by an experienced pathologist blinded to the experimental groups. For immunohistochemistry, formalin-fixed paraffin-embedded tissues were cut into 4-µm sections, and slides were stained with antibodies to identify IL-18 (MBL International, clone 39-3F) and neutrophils (7/4 monoclonal antibody, Invitrogen).

For transmission electron microscopy, cells were fixed in a solution of 2.0% paraformaldahyde with 2.5% glutaraldehyde in 0.1 M cacodylate buffer (pH 7.4). Cells were then embedded and sectioned for transmission electron microscopy by the Cell and Tissue Imaging Core Facility of St. Jude Children's Research Hospital.

For examination of LC3^{+} puncta numbers or colocalization with mitochondria by confocal microscopy, BMDCs were infected with IAV at 10 MOI or treated with 50 µM chloroquine (Calbiochem) 1 h after infection. After 18 h, cells were treated with 100 nM MitoTracker Orange CMTMRos (Invitrogen) for 30 min. Cells were then fixed in 4% paraformaldehyde in PBS with 100 mM HEPES buffer. Cells were permeablized with methanol at −20 °C for 5 min, washed 3× in DPBS and then blocked using 1× assay buffer (eBiosciences) with 0.1% Triton X-100 (Sigma-Aldrich) for 1 h. Cells were stained overnight at 4 °C with a 1:500 dilution of anti-LC3B antibody (Novus Biologicals, NB600-1384) in blocking buffer. Cells were washed 3× and then stained with Alexa Fluor 488 donkey anti-rabbit secondary (Invitrogen, A-21206) for 2 h in blocking buffer. Cells were washed an additional 3× and then mounted using Prolong GOLD with DAPI (Invitrogen) and examined on a Nikon C1Si laser-scanning confocal microscope. Data analysis was performed using Image J.

Generation of bone marrow chimeras. Wild-type (CD45.1^{+}) and *Ripk2*$^{-/-}$ (CD45.2^{+}) mice, were lethally irradiated with a split dose of 1,200 rads (800 rads then 400 rads), then injected with 5 × 10^6 bone marrow cells from the indicated donors. Mice were allowed to recover for 6 weeks to ensure successful engraftment. The extent of bone marrow reconstitution was verified by staining lymphocytes with anti-CD45.1 APC and anti-CD45.2 FITC (Biolegend, A20, 104) for congenic markers, and was always > 90%.

Cell signaling, caspase-1 activation and IL-18 production *in vitro*. Wild-type, *Nod2*$^{-/-}$ and *Ripk2*$^{-/-}$ BMDCs were differentiated in complete RPMI medium containing 10% heat-inactivated FBS and supplemented with 20 ng/ml murine GM-CSF at 37 °C in a humidified atmosphere containing 5% CO_2 for 7 d. Cells were mock-infected or infected at MOI of 10 with PR8 or MOI of 10 with X31 for 24 h or MOI of 10 with *L. monocytogenes* for 4–6 h in antibiotic-free medium. For treatment with NAC (Sigma-Aldrich) or mito-TEMPO (Enzo Life Sciences), BMDCs were infected with 10 MOI PR8 for 1 h and then fresh RPMI 1640 medium with 10% FBS containing the indicated concentrations of inhibitors was added. Other inhibitors, including glyburide (Sigma-Aldrich), rapamycin or SB203580 (Calbiochem) were also added 1 h after infection. Supernatants were collected 18–24 h later for ELISA, and cells were lysed in RIPA buffer with protease inhibitor and phosphatase inhibitor (Calbiochem), followed by boiling in SDS sample buffer and examination by immunoblot. Anti-caspase-1 (Adipogen, AG-20B-0042), anti-ULK1 (Sigma-Aldrich, A7481), anti-LC3B (Novus Biologicals, NB600-1384), and anti-pUlk1 Ser555 (Cell Signaling Technologies, D1H4) were used for immunoblot detection,

and equal loading was verified by blotting with anti-GAPDH or anti–β-tubulin (Cell signaling Technologies, D16H11, 9F3). HRP-labeled anti-rabbit or anti-mouse were obtained from Jackson ImmunoResearch (111-035-046, 115-036-072).

Overexpression and coimmunoprecipitation. The 293T cells were transfected using Lipofectamine 2000 (Invitrogen) or Xfect (Clontech) according to the manufacturer's protocol and collected 24 h after transfection for examination by coimmunoprecipitation and/or by immunoblot. For coimmunoprecipitation, 3–4 10-cm wells each were transfected with pCMV6-Kan/Neo-RIPK2 (Origene), pBK-flag-NOD2 or pCMV-3xMyc-ATG16L1 and cells were lysed after 24 h in DPBS with 1% NP40 with protease inhibitors and phosphatase inhibitors (Calbiochem). In some experiments, 293T cells were also infected with 10 MOI influenza A/PR/8/34 H1N1 1 h before transfection. Coimmunoprecipitation was performed overnight at 4 °C with protein A/G PLUS agarose beads (SantaCruz) and rabbit anti-RIPK2 (SantaCruz, H300), mouse anti-Flag (Sigma, M2) and rabbit anti-Myc (SantaCruz, A14). Immunoblot was then performed with rabbit anti-RIPK2 (SantaCruz, H300), rabbit anti-Flag (Sigma, F7425), rabbit anti-Myc (SantaCruz, A14) and Exactacruz HRP anti-rabbit secondary (SantaCruz, SC-45043).

Statistical analysis. Data are represented as mean ± s.e.m. Statistical significance was determined by a Student's *t*-test, one-way ANOVA for multiple comparisons, and Kaplan-Meier survival plot and LogRank test for survival data. Data for $LC3^+$ puncta were not normally distributed, and data were analyzed by the Mann-Whitney test. $P \leq 0.05$ was considered statistically significant.

46. Hoffmann, E., Krauss, S., Perez, D., Webby, R. & Webster, R.G. Eight-plasmid system for rapid generation of influenza virus vaccines. *Vaccine* **20**, 3165–3170 (2002).
47. Takeda, K. *et al.* Defective NK cell activity and Th1 response in IL-18-deficient mice. *Immunity* **8**, 383–390 (1998).
48. Huang, G. *et al.* Signaling via the kinase p38alpha programs dendritic cells to drive TH17 differentiation and autoimmune inflammation. *Nat. Immunol.* **13**, 152–161 (2012).
49. Kundu, M. *et al.* Ulk1 plays a critical role in the autophagic clearance of mitochondria and ribosomes during reticulocyte maturation. *Blood* **112**, 1493–1502 (2008).

doi:10.1038/ni.2563